The International Journal of Advanced Manufacturing Technology (2019) 105:4107–4121
https://doi.org/10.1007/s00170-019-03552-1

ORIGINAL ARTICLE

Design of powder nozzle for high resource efficiency in directed energy deposition based on computational fluid dynamics simulation

Shiho Takemura[1] · Ryo Koike[1] · Yasuhiro Kakinuma[1] · Yohei Sato[1] · Yohei Oda[2]

Received: 7 September 2018 / Accepted: 7 March 2019 / Published online: 22 March 2019

Abstract

Directed energy deposition (DED), an additive manufacturing process, is a suitable approach for freeform production with metallic materials. By generating a melt pool with a high-power laser beam, injected material powder is contentiously laminated on a baseplate by melting and solidifying. Although all supplied powder should be molten and solidified in order to reduce the material waste, powder distribution is difficult to converge owing to turbulence around the melt pool. Furthermore, an inappropriate powder supply easily leads to sputter generation, which also increases the material waste. In this study, the gas flow under a powder nozzle was analyzed by a computational fluid dynamics (CFD) simulation in order to achieve a high convergence in the powder supply. By measuring the powder distribution with a laser light sheet system and conducting deposition tests, the powder distribution and supply efficiency were experimentally evaluated. According to a gas-solid multiphase-flow simulation, the convergence distance of the powder flow should be shorter than the laser beam focus distance to improve the powder convergence with a lower gas-flow rate. Moreover, the powder nozzles were redesigned by taking the simulation results into consideration, and deposition tests were conducted to evaluate the powder supply efficiency, porosity rate, and penetration rate. The experimental result of the designed nozzle shows a clear improvement in the powder supply efficiency from 50.2 to 66.0%.

Keywords Additive manufacturing · Directed energy deposition · Powder nozzle · Resource efficiency · Computational fluid dynamics · Inconel 625

1 Introduction

Additive manufacturing (AM) provides several advantages to industries including a freedom of shaping, waste reduction of materials, and cost reduction for wide-variety and small-amount productions. These advantages in AM attract various kinds of industries including aerospace, automotive, and medical products [1]. For metals, two types of laser-based AM are widely used: so-called powder bed fusion (PBF) and directed energy deposition (DED). Compared with PBF, DED is a suitable approach to produce a large-scale freeform production because it achieves high efficiency with a high-power laser and requires no strict shielding system. Furthermore, this method is used to repair damaged components, to manufacture new components, and to apply wear- and corrosion-resistant coatings [2]. On the other hand, DED still has several problems, e.g., residual pore [3, 4], low shape accuracy [5, 6], and a reduction in the powder supply efficiency. In order to solve these problems, Zhong et al. tried to enhance the density of deposit and experimentally investigated the influence of process parameters such as the drying treatment of the powder, laser power, and nominal powder particle size on the porosity [3]. Manvatkar proposed an approach to improve the shape accuracy by developing a three-dimensional transient heat transfer and fluid flow model [5], and Lu et al. introduced a support vector machine to predict the building precision [6]. Focusing on the reduction of the powder supply efficiency, a complex interaction between the gas flow and the powder interferes with the movement of powder. As a result, some powder cannot reach the melt pool correctly. Therefore, the interaction between the gas flow and the powder movement should be

---

✉ Ryo Koike
koike@sd.keio.ac.jp

[1] Department of System Design Engineering, Keio University, 3-14-1, Hiyoshi, Kohoku-ku, Yokohama, Kanagawa 223-8522, Japan

[2] DMG MORI CO., LTD, 2-35-16 Meieki, Nakamura-ku, Nagoya, Aichi 450-0002, Japan

analyzed from the viewpoint of fluid dynamics in order to increase the material supply ratio to the melt pool.

A measurement of the dispersion of the powder flow under a powder nozzle is conducted experimentally in DED [7–10]. In these studies, the influence of any parameters on the powder feed behavior around the powder nozzle was confirmed by using a high-speed camera and a laser light sheet system.

In light of a computational fluid dynamics (CFD) simulation, a solid-gas multiphase flow in DED has been studied by many researchers [8, 9, 11–14]. Pan et al. introduced a 3D numerical model to evaluate the gravity-driven metal powder flow and optimized gas-flow rate and the geometries of a coaxial nozzle [8]. Zhu et al. investigated the effect of the deposited layer's height and width on the powder concentration and the convergence distance by using a numerical simulation with an axisymmetric model [11]. Balu et al. evaluated the characteristics of the powder flow, the geometries of four radial nozzles, and the carrier gas-flow rate with numerical and experimental approaches in a metal-ceramic laser-based powder deposition [12]. Moreover, Mazzucato et al. redesigned and evaluated the powder nozzles based on a computational method [9]. However, the results of CFD simulations have not been verified because these studies do not conduct real DED tests. In addition, these studies did not discuss the relationship between the gas-flow rates, nozzle geometry, and powder efficiency.

In this study, the influence of carrier and shield gas-flow rates on the convergence of the powder supply was evaluated by experiments and a CFD simulation. Moreover, based on a gas-solid multiphase-flow simulation, the shape of the powder nozzle was redesigned to achieve a high convergence of the powder supply into the melt pool. Moreover, improved powder nozzles were made by taking the results of a simulation analysis, and deposition tests were conducted in order to evaluate the powder supply efficiency. The designed nozzles clearly show a higher efficiency than the conventional nozzle in the powder supply.

2 Methodology

2.1 Directed energy deposition

Directed energy deposition is defined as an additive manufacturing process in which focused thermal energy is used to fuse materials by melting as they are being deposited according to the ASTM International standards [15]. In DED, the deposit is formed on a baseplate by supplying metal powder and irradiating the laser beam at the same time.

In this study, the powder nozzle contains a powder injection system and a laser irradiation device, and employs a coaxial-type nozzle having two flow paths. Figure 1 shows the appearance, and Fig. 2 shows the schematic of DED. As shown in Fig. 2, metal powder is injected to the melt pool by a carrier gas through the outer flow path, and shield gas is supplied through the inner flow path. Inactive gas such as argon is often used for the carrier and shield gas in order to prevent the oxidation of deposits. In addition, the path for the laser beam is ensured at the center of the coaxial nozzle.

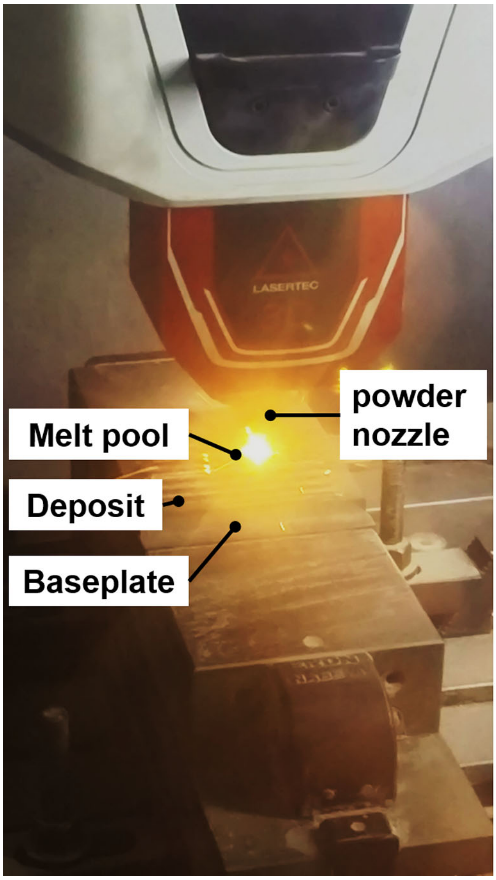

Fig. 1 Deposition by DED

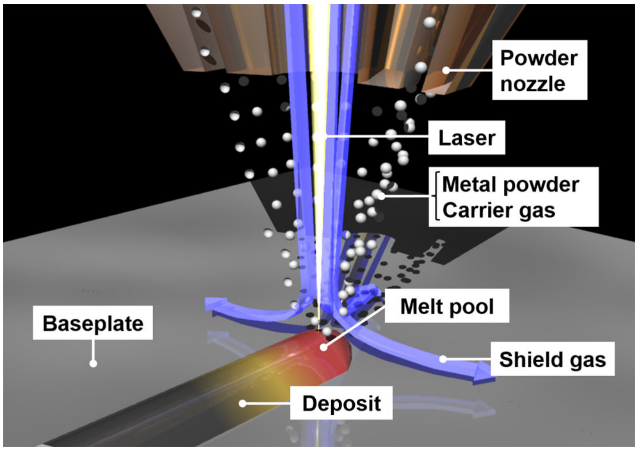

Fig. 2 Schematic of DED

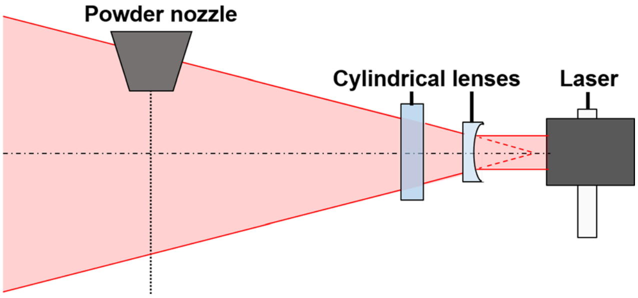

Fig. 3 Schematic of laser light sheet system

2.2 Numerical simulation

A gas-solid multiphase-flow simulation was conducted to analyze the powder movement around the powder nozzle. In this study, the Euler-Lagrange approach was applied, in which the gas and solid phases are treated as continuous and discrete phases, respectively.

2.2.1 Modeling of gas flow

In order to analyze the gas flow under the powder nozzle, both states of steady flow and turbulence should be considered synthetically. From this viewpoint, the gas flow is computed by solving a continuity equation and Navier-Stokes equation based on the time-averaging method known as Reynolds averaging, and applying the k- ε turbulent flow model. The Reynolds-averaged equations are given by Eqs. (1) and (2).

$$\frac{\partial \overline{u_i}}{\partial x_i}=0 \tag{1}$$

$$\frac{\partial \overline{u_i}}{\partial t}+\overline{u_j}\frac{\partial \overline{u_i}}{\partial x_j}=-\frac{1}{\rho}\frac{\partial \overline{p}}{\partial x_i}+\nu\frac{\partial^2 \overline{u_i}}{\partial {x_j}^2}-\frac{\partial \overline{{u_i}' {u_j}'}}{\partial x_j} \tag{2}$$

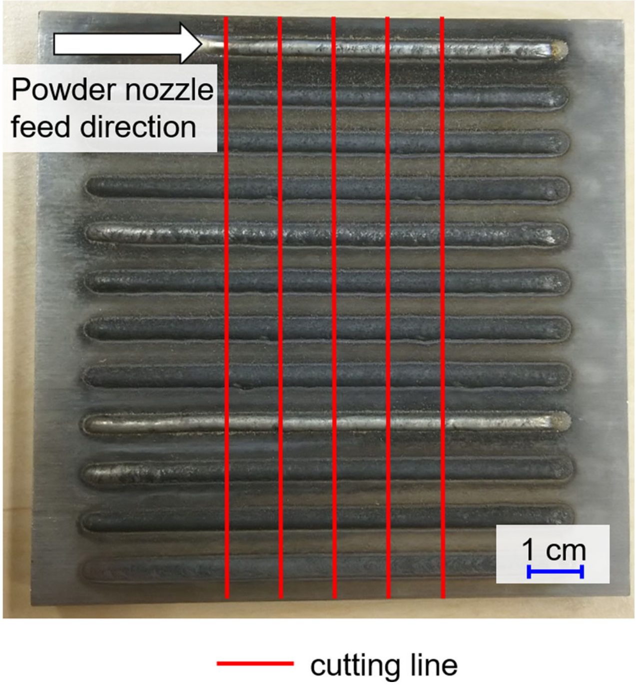

Fig. 5 Deposited object (single layer)

where u_i [m/s] is the flow velocity, x_i [m] is the Cartesian coordinate, t [s] is the time, ρ [kg/m^3] is the density, p [kg/m·s^2] is the pressure, ν [m^2/s] is the kinematic viscosity, and bar denotes the time average value. In Eq. (2), the first and second terms on the left side represent the time term and the convection term, respectively, and the terms on the right side represent the pressure term, viscosity term, and turbulent diffusion term in order.

In order to solve the equations, the k-ε model proposed by Launder and Spalding [16] is applied. This is the most commonly used method to complete turbulence models and is incorporated in most commercial CFD programs [17]. In this model, the turbulent viscosity μ_t [kg/(m·s)] is given as

$$\mu_t = C_\mu \rho \frac{k^2}{\varepsilon} \tag{3}$$

where C_μ is the model constant, k [m^2/s^2] is the turbulent kinetic energy, and ε [m^2/s^3] is the dissipation of kinetic energy of the turbulence. The conservation of the turbulent kinetic energy is expressed as

Fig. 4 Example images of powder flow. **a** Illuminated by LED light. **b** Illuminated by laser light sheet

(a) Illuminated by LED light (b) Illuminated by laser light sheet

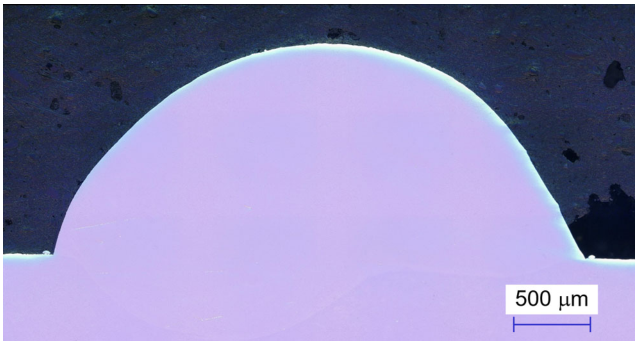

Fig. 6 Cross-sectional area

$$\frac{\partial(\rho k)}{\partial t}+\frac{\partial(\rho k u_i)}{\partial x_i}=\frac{\partial}{\partial x_j}\left\{\left(\mu+\frac{\mu_t}{\sigma_k}\right)\frac{\partial k}{\partial x_j}\right\}+\rho\overline{u_i{}'u_j{}'}\frac{\partial \overline{u_i}}{\partial x_j}-\rho\varepsilon \tag{4}$$

The conservation of the dissipation of kinetic energy of the turbulence is expressed as

$$\frac{\partial(\rho\varepsilon)}{\partial t}+\frac{\partial(\rho\varepsilon u_i)}{\partial x_i}=\frac{\partial}{\partial x_j}\left\{\left(\mu+\frac{\mu_t}{\sigma_\varepsilon}\right)\frac{\partial \varepsilon}{\partial x_j}\right\} \tag{5}$$
$$+\left(C_{\varepsilon 1}\rho\overline{u_i{}'u_j{}'}\frac{\partial \overline{u_i}}{\partial x_j}-C_{\varepsilon 2}\rho\varepsilon\right)\frac{\varepsilon}{k}$$

where $C_\mu = 0.09$, $\sigma_k = 1.0$, $\sigma_\varepsilon = 1.3$, $C_{\varepsilon 1} = 1.44$, and $C_{\varepsilon 2} = 1.92$ are the empirical constants.

2.2.2 Modeling of powder particle

In the Euler-Lagrange approach, the discrete phase is solved by tracking a large number of particles through the calculated flow field. The particle track is computed by a motion equation as follows:

$$\frac{du_p}{dt}=\frac{u-u_p}{\tau_r}+g\frac{\rho_p-\rho}{\rho_p} \tag{6}$$

where u_p [m/s] is the particle velocity, u [m/s] is the fluid velocity, ρ_p [kg/m^3] is the particle density, ρ [kg/m^3] is the fluid density, τ_r [s] is the particle relaxation time, and g [m/s^2] is the gravitational acceleration. Since the fluid density is much smaller than the particle density ($\rho/\rho_p \ll 1$), the drag force and the gravitational force dominantly work on the particles. Then, the particle relaxation time τ_r is calculated by

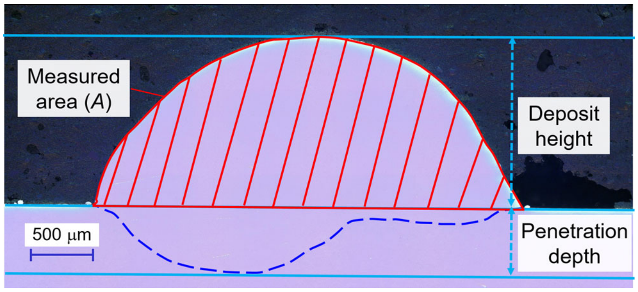

Fig. 8 Penetration depth

$$\tau_r=\frac{\rho_p d_p^2}{18\mu}\frac{24}{C_d Re_p} \tag{7}$$

where d_p [m] is the particle diameter, μ [kg/(m·s)] is the fluid viscosity, and Re_p is the particle Reynolds number. Re_p is defined as

$$Re_p=\frac{\rho d_p\left|u_p-u\right|}{\mu} \tag{8}$$

2.3 Laser light sheet system

In order to capture the powder distribution in the gas flow under the powder nozzle, a laser light sheet system was applied in this study. Figure 3 shows a schematic of the laser light sheet system. The laser was made into a sheet through by using cylindrical lenses. In this study, the thickness of the laser light sheet is designed to be 0.5 mm around the central axis of the powder nozzle. Figure 4 b shows an example image of powder flow captured by using this system. Compared to an image which powder flow is illuminated from the front by LED light (Fig. 4 a), Fig. 4 b can capture the distribution more appropriately, because it illuminates the cross section of the flow.

2.4 Evaluation for powder supply efficiency

In this study, the powder supply efficiency E_p was calculated from the cross-sectional area of the deposited object according to Eq. (9).

$$E_p=\frac{AF\rho_p}{f_p} \tag{9}$$

Fig. 7 Binarization. **a** Original image. **b** Preprocessed image. **c** Binary image

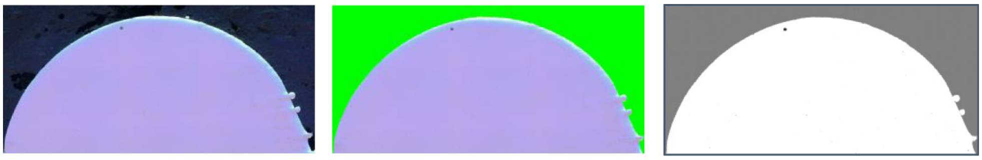
(a) Original image (b) Preprocessed image (c) Binary image

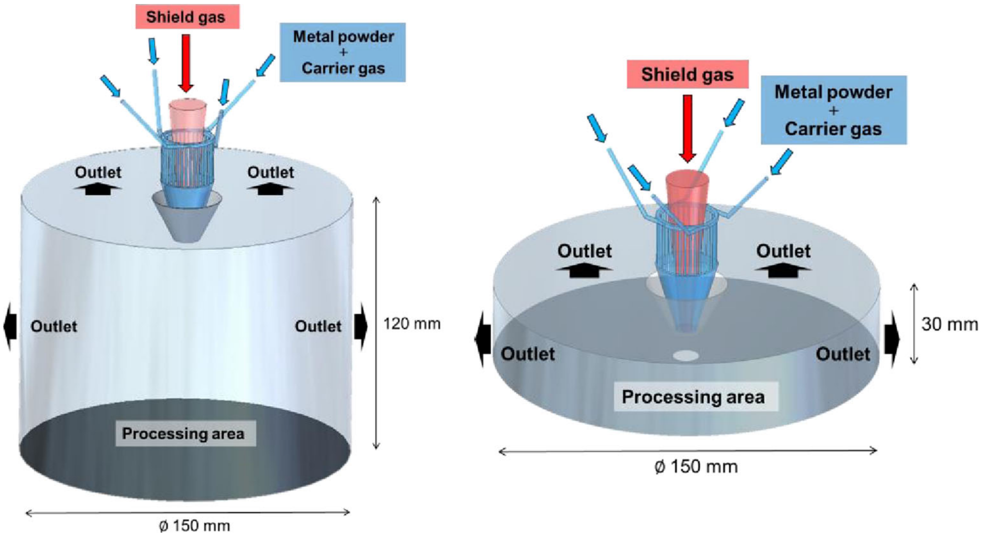

(a) Without baseplate (b) With baseplate

Fig. 9 Simulation model. **a** Without baseplate. **b** With baseplate

where A [mm^2] is the cross-sectional area, F [mm/min] is the powder nozzle feed rate, ρ_p [kg/m^3] is the material density, and f_p [kg/min] is the metal powder supply rate. In order to measure the cross-sectional area A, the deposited object was cut as shown in Fig. 5 with an abrasive water jet machine and is polished. Figure 6 shows a cross-sectional image of the deposited object as observed with a digital microscope.

Moreover, the residual pore in the deposited object is detrimental to the mechanical properties such as tensile strength, yield strength, and breaking elongation [4]. Therefore, the porosity rate should also be evaluated in the deposition tests. In the cross-sectional image, the non-evaluated area is distinguished from the evaluated area as shown in Fig. 7 b. In the next step, the preprocessed image is binarized, and the aggregate of black pixels is regarded as a pore area. At the end, the porosity rate is determined by comparing the number of total pixels and black pixels on the cross section in the binarized image.

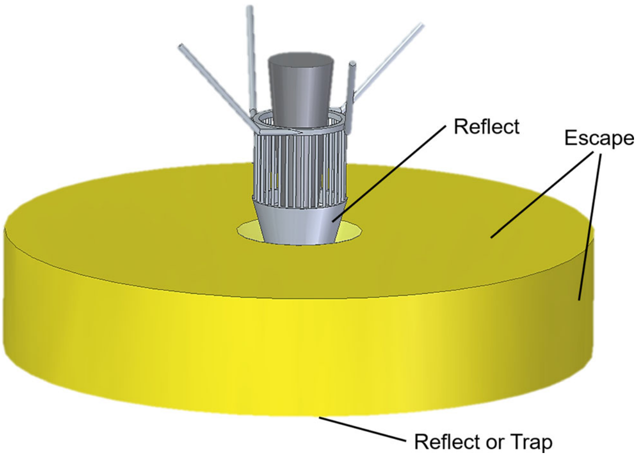

Fig. 10 Boundary conditions of discrete phase

In addition, melting metal material penetrates into the baseplate in DED. The dotted line in Fig. 8 indicates the edge of the penetrated area. In this study, penetration was evaluated by measuring and comparing the single-deposit height and the penetrated depth, as shown in Fig. 8. Moreover, the shaded area with red lines in Fig. 8 indicates the cross-sectional area in Eq. (9).

3 Simulation

3.1 Simulation model and conditions

To clarify the influence of the gas-flow rates on the powder distribution, a gas-solid multiphase-flow simulation was conducted by using CFD software (ANSYS Fluent 16.0, ANSYS, Inc.). In this study, two types of 3D–computer-aided design (CAD) model were used, as shown in Fig. 9. In order to compare the powder distribution in the measurement results with the laser sheet system, one model ensures the height of the processing area, as shown in Fig. 9 a. The other model shown in Fig. 9 b analyzes the powder distribution in the

Table 1 Analysis conditions

Carrier gas-flow rate	L/min	2, 3, 4, 6, 8, 10
Shield gas-flow rate	L/min	2, 4, 6
Powder feed rate	kg/min	18×10^{-3}
Fluid density	kg/m^3	1.784
Fluid viscosity	kg/(m·s)	2.22×10^{-5}
Particle density	kg/m^3	8440
Particle size	μm	53–105

Fig. 11 Turbulent flow under powder nozzle. **a** Carrier gas-flow rate 4 L/min. **b** Carrier gas-flow rate 10 L/min

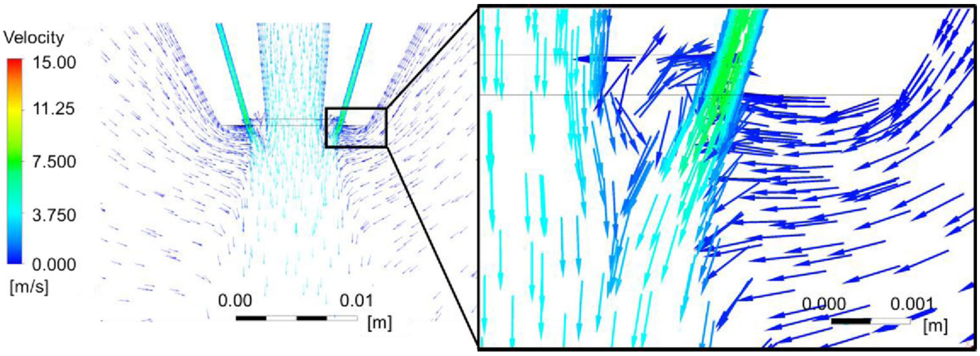

(a) Carrier gas flow rate 4 L/min

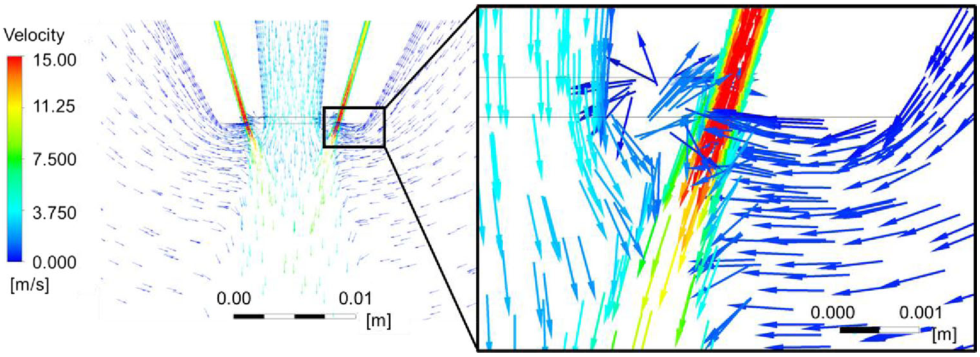

(b) Carrier gas flow rate 10 L/min

deposition process by assuming that there is a baseplate under the powder nozzle.

In order to conduct a simulation, the following boundary conditions for gas flow are applied:

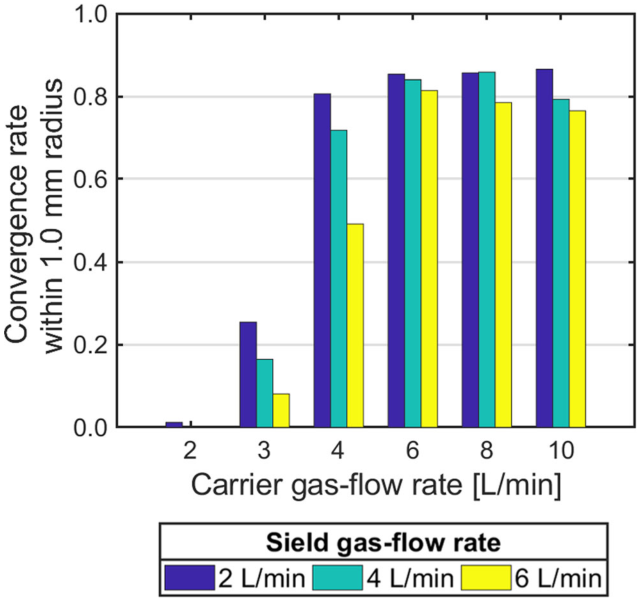

Fig. 12 Relationship between powder convergence rate and gas-flow rates

- At the shield and carrier gas inlets, each velocity is defined according to its flow rate.
- At the outlet, the gauge pressure is set to be zero.
- At the wall, the no-slip condition is applied.

Furthermore, boundary conditions of discrete phase are set as shown in Fig. 10. Particles are escaped from the side and upper surface of the deposition space. As to the bottom of the processing area, particles are reflected or trapped depending on the purpose of the simulation.

In addition, the following assumptions are taken into the simulation;

- Collisions among particles are not considered.

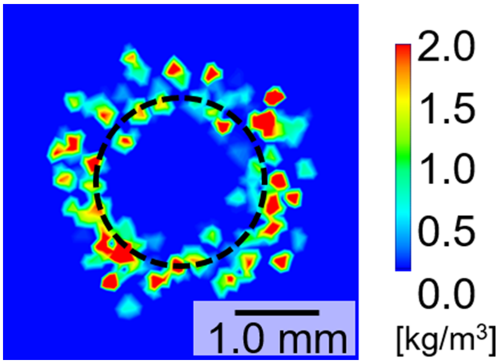

Fig. 13 Example of particle mass concentration on baseplate

Fig. 14 Direction of nozzle redesign. **a** Conventional nozzle. **b** Designed nozzle

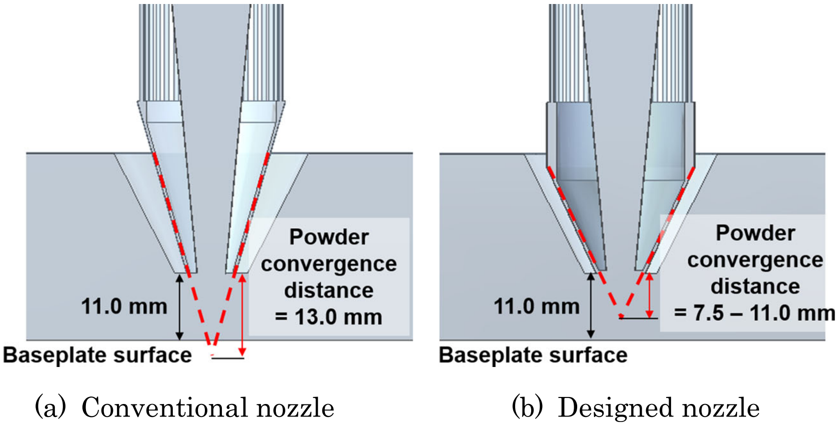

(a) Conventional nozzle (b) Designed nozzle

- A steady-state gas flow is considered.
- Particles' shape is assumed to be spherical.
- A Rosin-Rammler distribution is applied to particle diameters.
- Interaction between particles and the laser is not considered.

The simulation conditions are given in Table 1. The fluid density and viscosity were determined according to the physical properties of Argon [18], and the particle density was defined according to the physical properties of Inconel 625 [19].

Table 2 Analysis conditions

Carrier gas-flow rate	L/min	3, 4, 6, 8
Shield gas-flow rate	L/min	2, 4, 6
Convergence distance of powder flow	mm	7.5, 8.0, 8.5, 9.0, 9.5, 10.0, 10.5, 11.0, 13.0

3.2 Powder distribution analysis

Figure 11 shows the vector of the fluid velocity under the powder nozzle with a shield gas-flow rate of 4 L/min and carrier gas-flow rate of 4 and 10 L/min. In particular, the complex flow is confirmed around the outlet of the supply path. This result shows that the flow under the powder nozzle clearly becomes turbulent, and also indicates the validity of applying the turbulent flow model in this simulation.

To investigate the convergence of the powder flow on the baseplate, the 3D-CAD model shown in Fig. 9 b was also used in the CFD simulation. Figure 12 shows the relationship between the gas-flow rates and the convergence rate of the powder flow, which is defined as the ratio of the powder supply to the area within 1.0 mm from the center of the nozzle. This is shown in Fig. 13 with a dotted circle. The result shows that the convergence of the powder flow increases with a higher carrier gas-flow rate. This is because the particle velocity becomes higher with an increase in the carrier gas-flow rate.

Fig. 15 Particle mass concentration (on baseplate). **a** Convergence distance of 13.0 mm (conventional nozzle). **b** Convergence distance of 8.0 mm

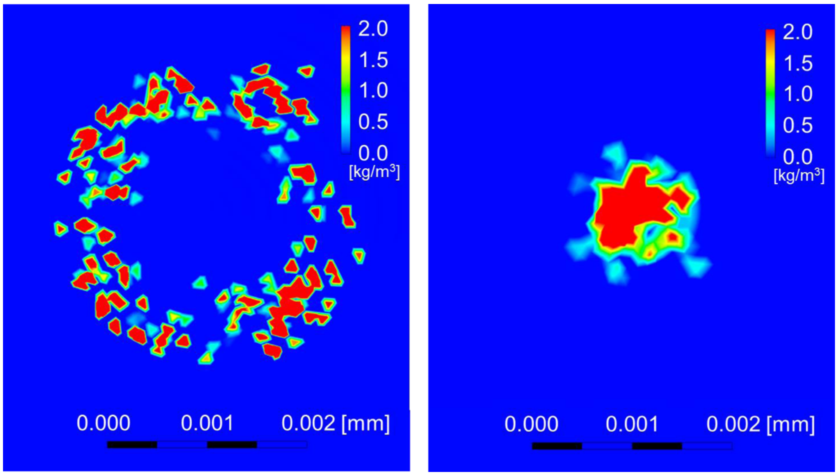

(a) Convergence distance of 13.0 mm (conventional nozzle) (b) Convergence distance of 8.0 mm

Fig. 16 Particle mass concentration (side view). **a** Convergence distance of 13.0 mm (conventional nozzle). **b** Convergence distance of 8.0 mm

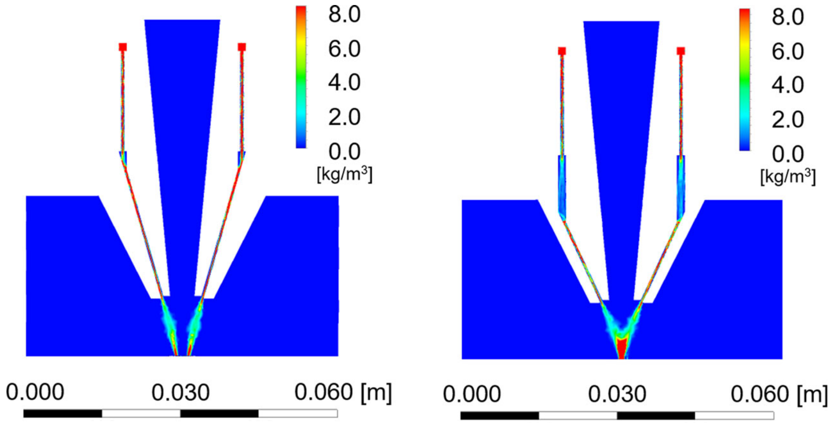

(a) Convergence distance of 13.0 mm (conventional nozzle)

(b) Convergence distance of 8.0 mm

In this case, the particle trajectory becomes straight, and the diffusion of the powder distribution can be suppressed. In particular, the convergence rate is almost zero with a carrier gas-flow rate of 2 L/min. Therefore, 2 L/min is inadequate for the carrier gas-flow rate in practical usage. Furthermore, for the shield gas-flow rate, the convergence rate decreases with an increase in the shield gas-flow rate except for a carrier gas-flow rate of 2 and 8 L/min, and it becomes lowest when the shield gas-flow rate is 6 L/min with all carrier gas-flow rate conditions. The shield gas disturbs the particle concentration at the center of the melt pool because the shield gas moves from the center to the outside of the powder nozzle (Fig. 2).

Fig. 17 Convergence rate with designed nozzles. **a** Carrier gas-flow rate of 3 L/min. **b** Carrier gas-flow rate of 4 L/min. **c** Carrier gas-flow rate of 6 L/min. **d** Carrier gas-flow rate of 8 L/min

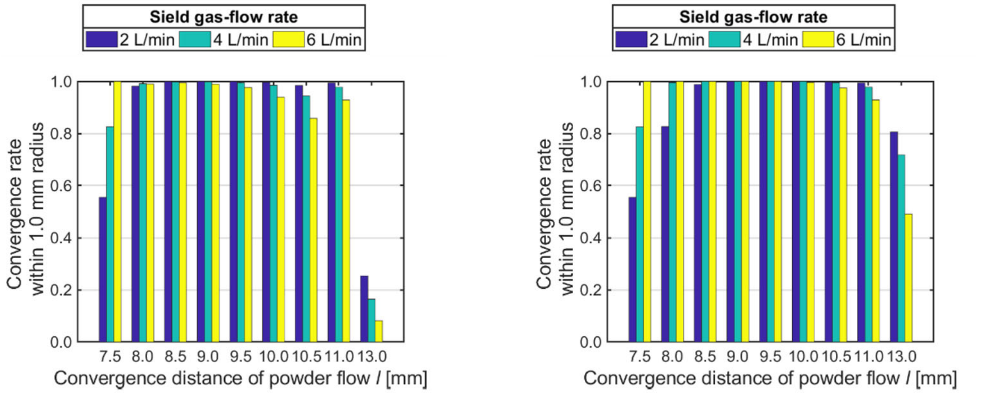

(a) Carrier gas-flow rate of 3 L/min

(b) Carrier gas-flow rate of 4 L/min

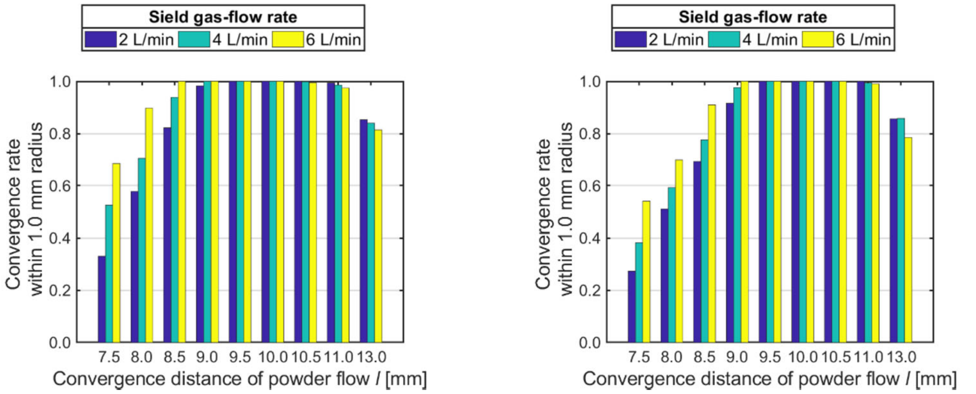

(c) Carrier gas-flow rate of 6 L/min

(d) Carrier gas-flow rate of 8 L/min

Fig. 18 Particle mass concentration (side view). **a** Carrier gas-flow rate of 3 L/min. **b** Carrier gas-flow rate of 8 L/min

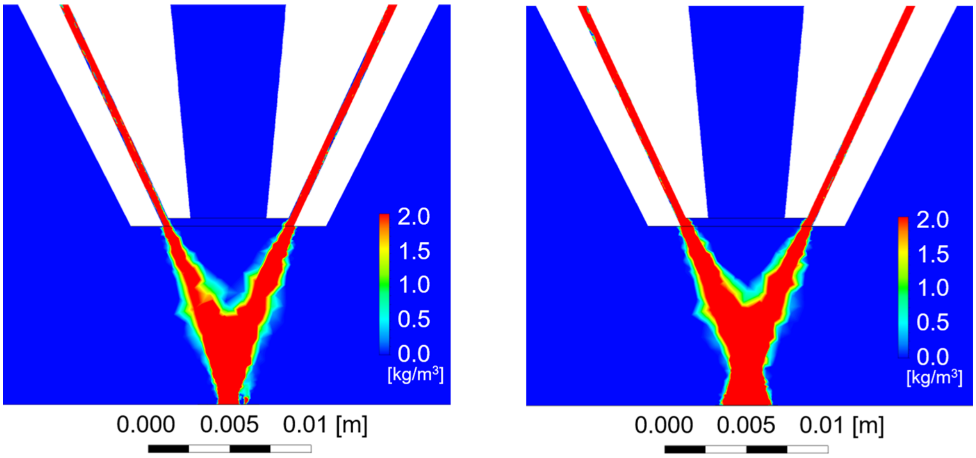

(a) Carrier gas-flow rate of 3 L/min (b) Carrier gas-flow rate of 8 L/min

3.3 Enhancement of convergence in powder supply

In this study, the powder nozzle was redesigned to achieve high convergence in the powder supply. In a deposition with a conventional powder nozzle, the distance between the powder nozzle and the baseplate surface was set to be 11.0 mm, whereas the convergence distance of the powder flow was designed to be 13.0 mm (Fig. 14 a). Although this difference was determined from an experimental evaluation, it caused a defocus of the powder flow on the melt pool. From this aspect, the convergence distance of the powder flow should be optimized theoretically based on the CFD simulation. In this study, 3D-CAD powder nozzles with eight types of convergence distances shorter than 11.0 mm were created (Fig. 14b), and a CFD simulation was conducted. The simulation conditions are given in Table 2.

Figure 17 shows the convergence rates with different carrier gas-flow rates. As shown in (a), all designed nozzles show a higher convergence than the conventional nozzle. In (b), all designed nozzles show a higher convergence, although this depends on the shield gas-flow rate. These results match the powder distributions shown in Figs. 15 and 16. In Fig. 17 c and d, although the designed nozzles whose convergence distances are greater than 9.0 mm show better convergence than those of the conventional nozzle, the convergence rate decreases with the shorter-convergence-distance nozzles. These results also indicate that a higher carrier gas-flow rate results in a longer convergence distance of the powder flow.

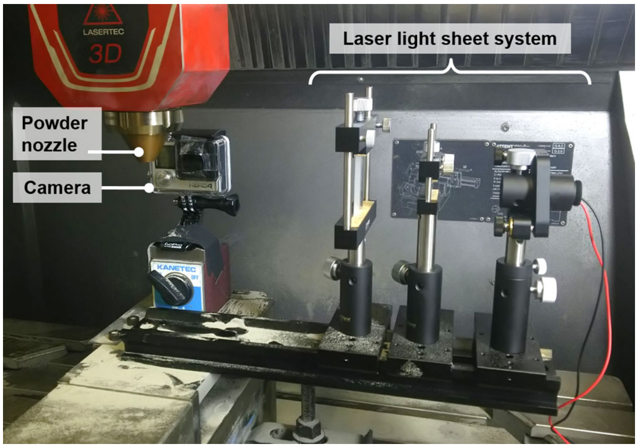

Fig. 19 Experimental setup

Figure 18 shows the particle mass concentration on the cross-sectional area of the powder flow. The powder distribution spreads with a high carrier gas supply of 8 L/min, as shown in (b). With an increase in the carrier gas-flow rate, the velocity of the powder becomes so high that the powder trajectories show the cross point not on the baseplate but near the convergence point. From these results, not only the convergence distance but also the carrier gas supply should be interactively considered to concentrate the powder distribution at the center of the baseplate effectively.

4 Experiment

4.1 Measurement of powder distribution

4.1.1 System configuration

To confirm the validity of the simulation results, a measurement of the powder distribution was conducted. A five-axial

Table 3 Powder feed conditions

Carrier gas-flow rate	L/min	2, 3, 4, 6, 8, 10
Shield gas-flow rate	L/min	2, 4, 6
Metal powder feed rate	kg/min	18×10^{-3}
Frame rate	fps	30
Number of pixels		1920 ×1080

Fig. 20 Image processing. **a** Original image. **b** Averaged grayscale image. **c** Luminance line

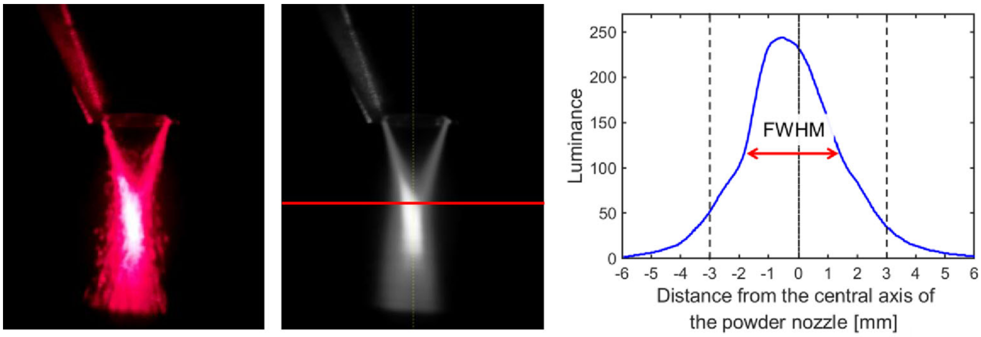

(a) Original image

(b) Averaged grayscale image

(c) Luminance line

combined machining center (LASERTEC 65 3D, DMG MORI CO., LTD.), including a DED function, was used in this study. Figure 19 shows the experimental setup. The powder flow was captured for 10 s in each condition by using a laser light sheet system and a camera. Furthermore, nickel-based alloy (Inconel 625) powder, whose diameter is 53–105 μm, was used. The experiments were conducted under various combinations of gas-flow rates as given in Table 3.

Figure 20 a shows an original image obtained in this experiment. To evaluate the powder distribution quantitatively, the captured image was analyzed according to its luminosity distribution. The captured images for 10 s were converted into

Fig. 21 Luminance line. **a** Shield gas-flow rate of 2 L/min. **b** Shield gas-flow rate of 4 L/min. **c** Shield gas-flow rate of 6 L/min

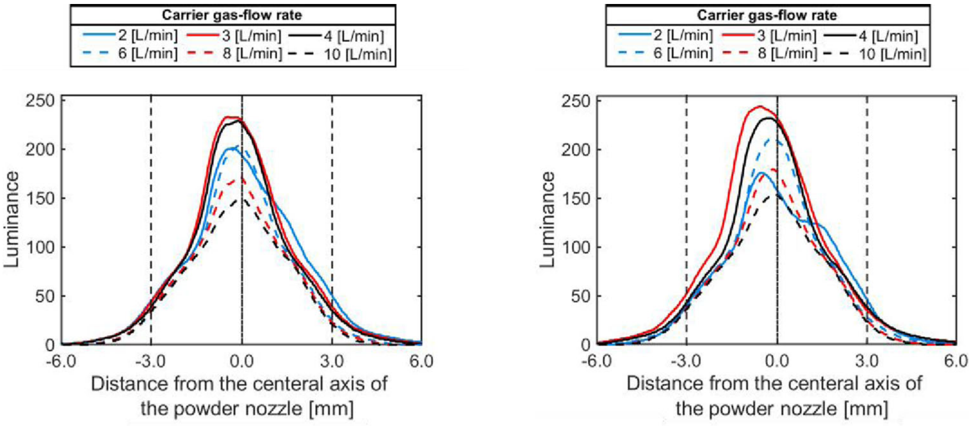

(a) Shield gas-flow rate of 2 L/min

(b) Shield gas-flow rate of 4 L/min

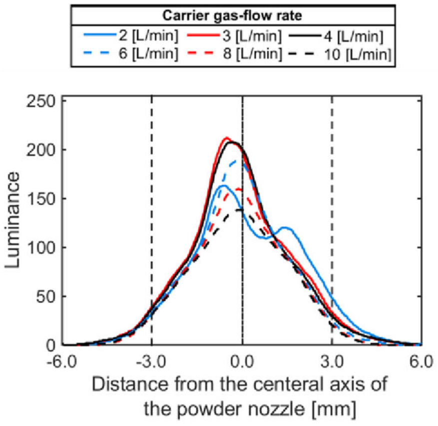

(c) Shield gas-flow rate of 6 L/min

Fig. 22 Relationship between full width at half maximum of powder flow and gas-flow rates

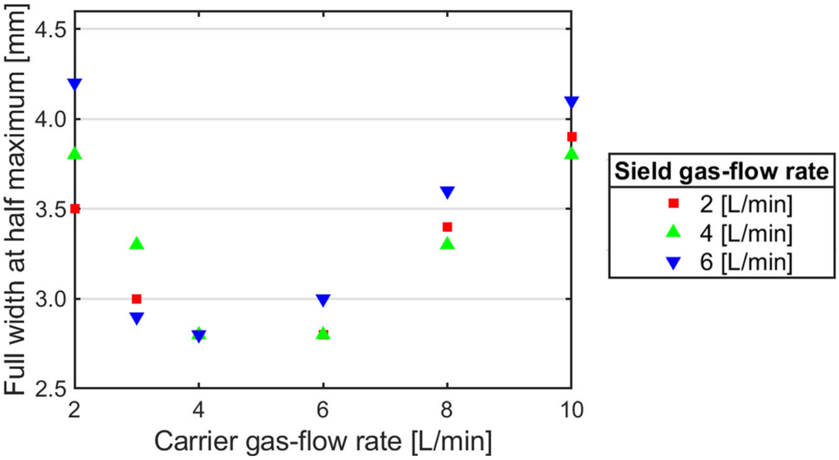

grayscale images based on their luminosity, and an averaged grayscale image such as that in Fig. 20 b was obtained. In addition, the luminosity on the horizontal red line, corresponding to the height of the deposition point, was extracted and summarized as shown in Fig. 20 c. In this study, the full width at half maximum (FWHM) of the luminance line was measured, and each powder supply condition was compared.

4.1.2 Evaluation of convergence in powder supply

Figure 21 shows the luminance line for each powder supply condition. Along with these results, the FWHM was measured and is summarized in Fig. 22. When the carrier gas-flow rate is lower than 4 L/min, the FWHM decreases with an increase in the carrier gas. On the other hand, when the carrier gas-flow rate is higher than 4 L/min, the FWHM becomes larger with an increase in the carrier gas-flow rate. Furthermore, Fig. 22 indicates that the shield gas-flow rate rarely influences the FWHM as compared with the carrier gas-flow rate.

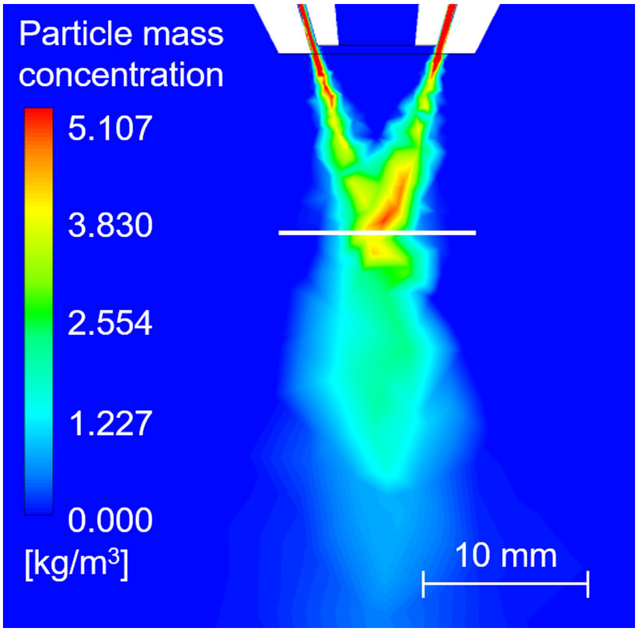

Fig. 23 Particle mass concentration on cross-sectional area of powder flow

4.1.3 Comparison with simulation

The experimental results in Section 4.1.2 are compared with the results of a simulation which uses a 3D-CAD model with-

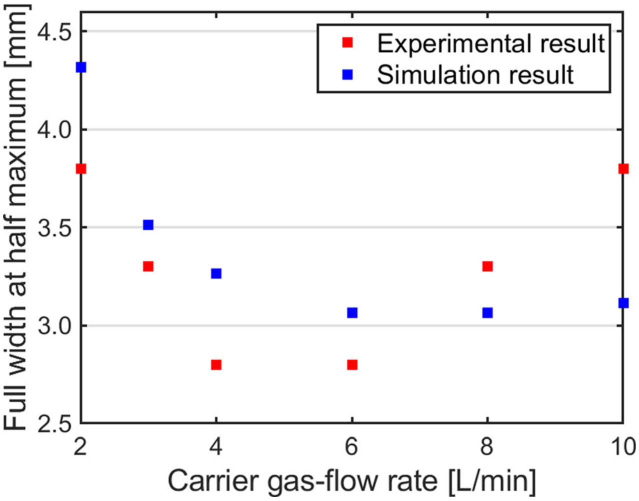

Fig. 24 Comparison with simulation result (shield gas-flow rate of 4 L/min)

Table 4 Deposition conditions for conventional nozzle

Carrier gas-flow rate	L/min	2, 3, 4, 6, 8, 10
Shield gas-flow rate	L/min	2, 4, 6
Laser power	W	1600
Powder nozzle feed rate	mm/min	400
Metal powder feed rate	kg/min	25×10^{-3}
Number of layers		1
Baseplate material		SUS304

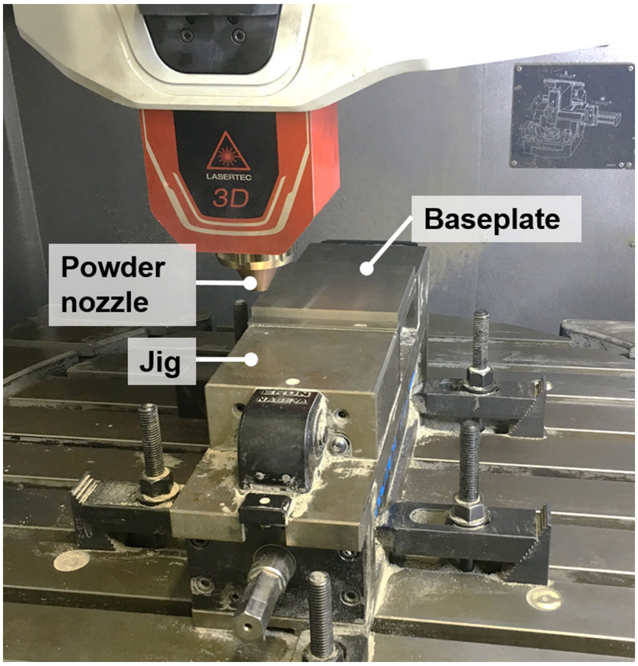

Fig. 25 Experimental setup

out a baseplate (Fig. 9 a). To obtain the simulation results corresponding to the experimental results of FWHM shown in Fig. 22, the particle mass concentration on the cross-sectional area of the powder flow given in Fig. 23 was used. At the white horizontal line, which is located at 11 mm below the powder nozzle in Fig. 23, the particle mass concentration was extracted and the FWHM of its distribution was measured. Figure 24 shows the experimental and simulation results of the FWHM with a shield gas-flow rate of 4 L/min. In the results of the experiment and simulation, the FWHM decreases with an increase in the carrier gas when the carrier gas-flow rate is lower than 4 L/min. Thus, it can be said that the tendencies of the simulation and experimental results almost match. However, in the simulation results, the FWHM becomes constant at a carrier gas-flow rate higher than 6 L/min, although the FWHM becomes larger in the experimental result. As Fig. 21 indicates, the overall luminance is lower with a higher carrier gas-flow rate owing to the higher powder velocity. The decline in overall luminance causes a noise in the detected data depending on the camera sensitivity. Consequently, the luminance distribution becomes vague, and the difference between the results of the simulation and experiment is generated.

4.2 Deposition test

4.2.1 Setup

In order to evaluate the influence of the gas-flow rates and the geometry of the powder nozzle on the powder supply efficiency, various deposition tests were conducted. First, to evaluate the influence of the gas-flow rates, deposition tests were conducted with the conventional nozzle under the conditions given in Table 4. Figure 25 shows the experimental setup.

4.2.2 Conventional nozzle

Figure 26 shows the relationship between the powder supply efficiency and the gas-flow rates. Each error bar denotes the maximum and minimum values for 15 samples. The powder supply efficiency E_p increases when the carrier gas-flow rate is 3 L/min for all conditions of the shield gas-flow rate. Furthermore, E_p gradually decreases at a higher carrier gas-flow rate. With a carrier gas-flow rate of 2 L/min, E_p is clearly low. This is because the supply path is jammed with powder owing to a shortage of the carrying force, as mentioned in the simulation results (Chapter 3.3). Although the convergence of the powder flow increases at a higher carrier gas-flow rate in the simulation results of the model with a baseplate, the

Fig. 26 Relationship between powder supply efficiency and gas-flow rates

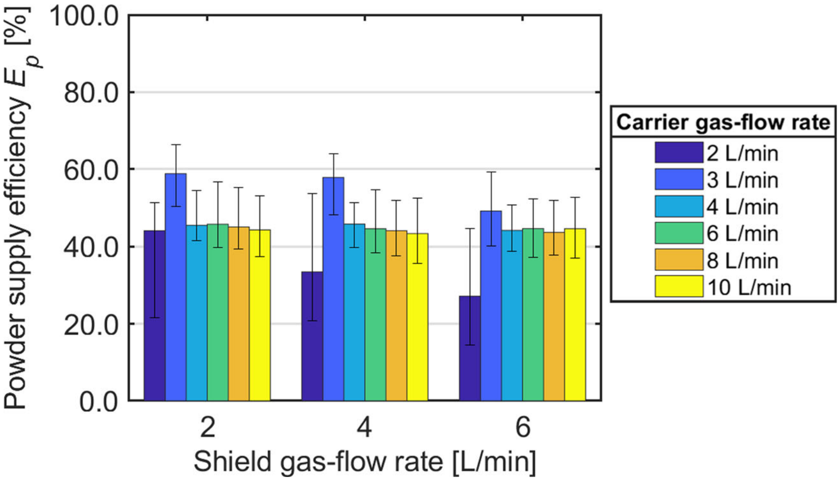

Fig. 27 Sputter generation. **a** Carrier gas-flow rate of 3 L/min. **b** Carrier gas-flow rate of 4 L/min. **c** Carrier gas-flow rate of 8 L/min

(a) Carrier gas-flow rate of 3 L/min (b) Carrier gas-flow rate of 4 L/min

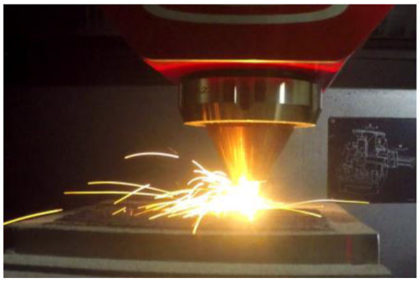

(c) Carrier gas-flow rate of 8 L/min

deposition results do not match. This difference is initiated by sputter generation from the melt pool. Figure 27 shows the sputter generated during the deposition, and it indicates that the number of sputters suddenly increases with an increase in the carrier gas-flow rate. Therefore, in order to improve the powder supply efficiency, enhancement of the powder-flow convergence and suppression of the sputter generation are needed.

4.2.3 Designed nozzles

According to the simulation results, it is confirmed that shortening the convergence distance of the powder flow is effective in enhancing the powder convergence. Moreover, from the results of the deposition tests, it becomes clear that the carrier gas-flow rate should be lower to improve the powder supply efficiency in terms of sputter suppression. Therefore, four powder nozzles with convergence distances of 7.5, 8.0, 8.5, and 9.0 mm are made. These convergence distances are selected because the high convergence is obtained stably with lower carrier gas-flow rates such as 3 and 4 L/min in Fig. 17, and an obvious difference is expected when compared with the conventional nozzle. By using the designed nozzles, deposition tests were conducted. The deposition conditions are given in Table 5.

Figure 28 shows the relationship between the powder supply efficiency E_p and the convergence distance. Each error bar denotes the maximum and minimum values for five samples. All E_p with designed nozzles are higher than that of the conventional nozzle. In particular, the highest E_p is 66.0% when using the 8.0-mm powder nozzle at a carrier gas-flow rate of 4 L/min. From this result, the improvement of the powder nozzle design by shortening the convergence distance of the powder flow is certainly effective in enhancing the powder supply efficiency.

In this study, the porosity rate and penetration rate were also measured to evaluate the influence of the nozzle geometry on the deposit characteristics. Figure 29 shows the relationship between the porosity rate and the convergence distance. Except for the results of the 8.5- and 9.0-mm powder nozzles at a carrier gas-flow rate of 3 L/min, the porosity rate becomes worse than that of the conventional nozzle. Moreover, the porosity rate becomes highest when using the 8.0-mm powder nozzle, which shows the highest powder supply efficiency in Fig. 28. Our previous work has shown that higher powder supply leads to higher porosity rate due to the lower heat input per unit volume [20]. Therefore, the increase in the powder supply efficiency affects the porosity rate owing to the increase in the necessary energy for melting the powder completely, and the adjustment of laser power would be necessary to enhance the production quality.

Table 5 Deposition conditions for designed nozzles

Carrier gas-flow rate	L/min	3, 4
Shield gas-flow rate	L/min	2
Convergence distance	mm	7.5, 8.0, 8.5, 9.0, 13.0
Laser power	W	1600
Powder nozzle feed rate	mm/min	400
Metal powder feed rate	kg/min	18×10^{-3}
Number of layer		1
Baseplate material		SUS304

Fig. 28 Comparison of powder supply efficiency between conventional and improved nozzles

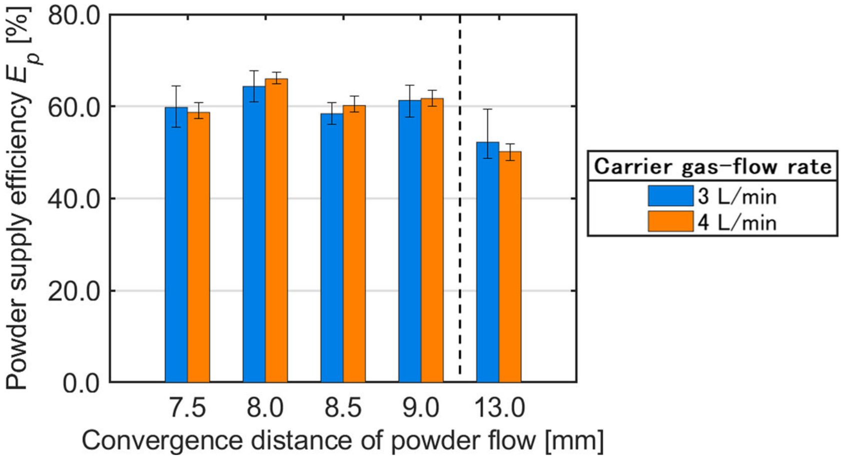

Fig. 29 Comparison of porosity rate between conventional and improved nozzles

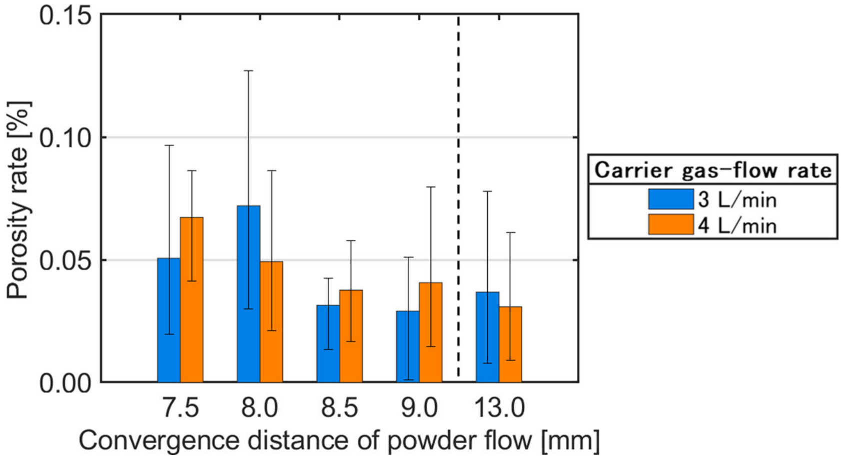

Figure 30 shows the relationship between the penetration rate and the convergence distance. The penetration rate of deposits made by using the designed nozzles is 17.8–36.2% and is lower than the results for the conventional nozzle. To shorten the powder convergence distance, the angle of the path which metal powder goes through was designed to be gentle, which causes a decrease in the downward force of the powder. As a result, the penetration rate became lower by using the designed nozzles.

Fig. 30 Comparison of penetration rate between conventional and improved nozzles

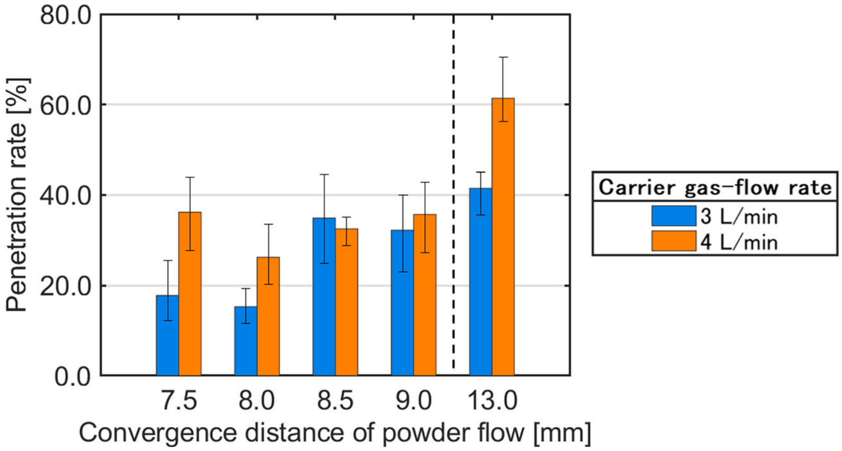

5 Conclusion

To enhance the powder supply efficiency in DED, the influence of the gas-flow rates and powder nozzle geometry on the convergence of the powder supply was evaluated by a CFD simulation. Furthermore, based on the simulation results, the powder nozzle was redesigned and experimentally evaluated. The obtained results are summarized as follows:

1. The CFD simulation indicates that the convergence of the powder flow increases with a higher carrier gas-flow rate because of higher particle velocity. In addition, the shield gas disturbs the particles from concentrating at the center of the melt pool.
2. The result of the CFD simulation indicates that shortening the convergence distance of the powder flow is effective in improving the convergence of the powder flow. In addition, the convergence distance of the powder flow that shows a high convergence became longer with an increase in the carrier gas-flow rate.
3. By conducting a deposition test, it was clarified that the powder-flow convergence and sputter suppression should be considered simultaneously to enhance the powder supply efficiency.
4. Deposition tests were also conducted by using the designed nozzle. The highest E_p was 66.0% by using an 8.0-mm powder nozzle with a carrier gas-flow rate of 4 L/min. Furthermore, the porosity and penetrate were also evaluated. The results indicated that an increase in the powder supply efficiency affected the porosity rate, and the penetration rate became smaller when using the designed nozzles.

References

1. Schmidt M, Merklein M, Bourell D, Dimitrov D, Hausotte T, Wegener K, Overmeyer L, Vollertsen F, Levy GN (2017) CIRP annals - manufacturing technology laser based additive manufacturing in industry and academia. CIRP Ann Manuf Technol 66:561–583. https://doi.org/10.1016/j.cirp.2017.05.011
2. Dutta B, Singh V, Natu H et al (2009) Direct metal deposition. Adv Mater Process 167:33–36
3. Zhong C, Gasser A, Schopphoven T, Poprawe R (2015) Experimental study of porosity reduction in high deposition-rate laser material deposition. Opt Laser Technol 75:87–92. https://doi.org/10.1016/j.optlastec.2015.06.016
4. Zhong C, Gasser A, Kittel J, Wissenbach K, Poprawe R (2016) Improvement of material performance of Inconel 718 formed by high deposition-rate laser metal deposition. Mater Des 98:128–134. https://doi.org/10.1016/j.matdes.2016.03.006
5. Manvatkar V, De A, DebRoy T (2015) Spatial variation of melt pool geometry, peak temperature and solidification parameters during laser assisted additive manufacturing process. Mater Sci Technol 31:924–930. https://doi.org/10.1179/1743284714Y.0000000701
6. Lu ZL, Li DC, Lu BH, Zhang AF, Zhu GX, Pi G (2010) The prediction of the building precision in the Laser Engineered Net Shaping process using advanced networks. Opt Lasers Eng 48:519–525. https://doi.org/10.1016/j.optlaseng.2010.01.002
7. Tan H, Zhang F, Wen R, Chen J, Huang W (2012) Experiment study of powder flow feed behavior of laser solid forming. Opt Lasers Eng 50:391–398. https://doi.org/10.1016/j.optlaseng.2011.10.017
8. Pan H, Sparks T, Thakar YD, Liou F (2006) The investigation of gravity-driven metal powder flow in coaxial nozzle for laser-aided direct metal deposition process. J Manuf Sci Eng 128:541. https://doi.org/10.1115/1.2162588
9. Mazzucato F, Tusacciu S, Lai M, Biamino S, Lombardi M, Valente A (2017) Monitoring approach to evaluate the performances of a new deposition nozzle solution for DED systems. Technologies 5:29. https://doi.org/10.3390/technologies5020029
10. Lin J (1999) Concentration mode of the powder stream in coaxial laser cladding. Opt Laser Technol 31:251–257. https://doi.org/10.1016/S0030-3992(99)00049-3
11. Zhu G, Li D, Zhang A, Tang Y (2011) Numerical simulation of metallic powder flow in a coaxial nozzle in laser direct metal deposition. Opt Laser Technol 43:106–113. https://doi.org/10.1016/j.optlastec.2010.05.012
12. Balu P, Leggett P, Kovacevic R (2012) Parametric study on a coaxial multi-material powder flow in laser-based powder deposition process. J Mater Process Technol 212:1598–1610. https://doi.org/10.1016/j.jmatprotec.2012.02.020
13. Liu H, He XL, Yu G, Wang ZB, Li SX, Zheng CY, Ning WJ (2015) Numerical simulation of powder transport behavior in laser cladding with coaxial powder feeding. Sci China Phys Mech Astron 58. https://doi.org/10.1007/s11433-015-5705-4
14. Ibarra-Medina J, Pinkerton AJ (2010) A CFD model of the laser, coaxial powder stream and substrate interaction in laser cladding. Phys Procedia 5:337–346. https://doi.org/10.1016/j.phpro.2010.08.060
15. ASTM International (2013) F2792-12a - standard terminology for additive manufacturing technologies. Rapid Manuf Assoc:10–12. https://doi.org/10.1520/F2792-12A.2
16. Launder BE, Spalding DB (1972) Lectures in mathematical models of turbulence. Academic Press, London
17. Pope SB (2000) Turbulent flows. Cambridge University Press, New York
18. Rumble JR (2017) CRC handbook of chemistry and physics, 98th edn. Taylor & Francis Group, Boca Raton
19. Gale WF (2004) Smithells metals reference book eighth edition. Butterworth-Heinemann, Burlington
20. Koike R, Misawa T, Kakinuma Y, Oda Y (2018) Basic study on remelting process to enhance density of Inconel 625 in directed energy deposition. Int J Autom Technol 12:424–433